

The dynamics of internal working surfaces in MHD jets

Fabio De Colle

Dublin Institute for Advanced Studies (DIAS), 31 Fitzwilliam Place, Dublin 2, Ireland

`fdc@cp.dias.ie`

and

Alejandro C. Raga and Alejandro Esquivel

Instituto de Ciencias Nucleares, UNAM, A. Postal 70-543, 04510 México, México

`raga, esquivel@nucleares.unam.mx`

ABSTRACT

The dynamical effects of magnetic fields in models of radiative, Herbig-Haro (HH) jets have been studied in a number of papers. For example, magnetized, radiative jets from variable sources have been studied with axisymmetric and 3D numerical simulations. In this paper, we present an analytic model describing the effect of a toroidal magnetic field on the internal working surfaces that result from a variability in the ejection velocity. We find that for parameters appropriate for HH jets the forces associated with the magnetic field dominate over the gas pressure force within the working surfaces. Depending on the ram pressure radial cross section of the jet, the magnetic field can produce a strong axial pinch, or, alternatively, a broadening of the internal working surfaces. We check the validity of the analytic model with axisymmetric numerical simulations of variable, magnetized jets.

Subject headings: ISM: kinematics and dynamics – ISM: jets and outflows – ISM: Herbig-Haro objects – stars: magnetic fields – stars: pre-main sequence – winds, outflows

1. Introduction

It is now relatively certain that some Herbig-Haro (HH) jets have knot structures which are the result of a time-variability in the ejection. For example, the observations of some

jets with organized structures of knots of different sizes (e. g., HH 30, 34 and 111, see Esquivel et al. 2007, Raga et al. 2002 and Masciadri et al. 2002) can be reproduced surprisingly well with variable ejection jet models. In the present paper, we study the effect of the presence of a magnetic field on the evolution of a variable jet.

It is still an open question to what extent magnetic fields are important in determining the dynamics of HH jets. The associated problem of radiative, MHD jets has been explored in some detail in the existing literature. Cerqueira et al. (1997), and Cerqueira & de Gouveia Dal Pino (1999) computed 3D simulations of radiative, MHD jets with different magnetic field configurations (at the injection point). Frank et al. (1998) carried out axisymmetric simulations of similar flows.

The problem of an MHD, radiative jet ejected with a time-variable velocity was explored with axisymmetric simulations by Gardiner & Frank (2000); Gardiner et al. (2000); Stone & Hardee (2000); O’Sullivan & Ray (2000); Frank et al. (2000); De Colle & Raga (2006) and Hartigan et al. (2007). Variable, MHD jets were also explored with 3D simulations by Cerqueira & de Gouveia Dal Pino (2001a,b). The general conclusions that can be obtained from these simulations is that the internal working surfaces produced by the ejection variability are not affected strongly by a poloidal magnetic field. On the other hand, if the magnetic field is toroidal (or, alternatively, has a strong toroidal component), the material within the working surfaces of the jet flow has a stronger concentration towards the jet axis.

Gardiner & Frank (2000) showed that in a variable ejection velocity jet the “continuous jet beam” sections in between the working surfaces have a low toroidal magnetic field, which grows in strength quite dramatically when the material goes through one of the working surface shocks into one of the knots. In the present paper, we present a simple, analytic model from which we obtain the conditions under which the toroidal magnetic field produces an axial compression of the internal working surfaces. This analytic model is presented in §2. In §3, we present axisymmetric numerical simulations in which we compare the working surfaces with and without a toroidal magnetic field, showing the effect described by the analytic model. Finally, in §4 we present our conclusions.

2. The radial motion of the material within an internal working surface

2.1. General considerations

A time-variability in the ejection velocity leads to the formation of two-shock “internal working surfaces” which travel down the jet flow. In a frame of reference that moves with the working surface, the flow takes the configuration shown in Figure 1, with material entering

the shocked layer from both the upstream and downstream directions.

Let us consider an internal working surface within a cylindrically symmetric jet with a toroidal magnetic field configuration. The material in the jet beam cross section or within the working surface is subject to two radial forces: the magnetic pinch force

$$F_m = -\frac{B}{4\pi r} \frac{d}{dr}(rB), \quad (1)$$

where B is the toroidal magnetic field and r the cylindrical radius, and the force due to the pressure gradient

$$F_p = -\frac{dP}{dr}, \quad (2)$$

where P is the gas pressure. The cross section of the jet is in lateral equilibrium when $F = F_m + F_p = 0$, it will be subject to a lateral expansion when $F > 0$ and to a compression when $F < 0$.

Let us now assume that the jet beam has a generic cross section of the form

$$\rho(r) = \rho_0 \underline{\rho}(r), \quad (3)$$

$$B(r) = B_0 \underline{B}(r), \quad (4)$$

$$v(r) = v_0 \underline{v}(r), \quad (5)$$

where $\rho(r)$ is the density, $B(r)$ the magnitude of the (toroidal) magnetic field, and $v(r) = v_j - v_w$ is the relative velocity with which the jet material (moving at a velocity v_j) enters the working surface (which moves at a velocity v_w), see Figure 1. The constants ρ_0 , B_0 and v_0 correspond to characteristic values of the respective quantities, and $\underline{\rho}(r)$, $\underline{B}(r)$ and $\underline{v}(r)$ are dimensionless functions of the radius giving the radial dependence of the flow variables from $r = 0$ (the symmetry axis) out to $r = r_j$ (the outer radius of the jet beam). In principle, these three dimensionless functions are of order one unless very strong changes in the flow variables occur across the jet cross section.

Let us now consider that the material goes through the “Mach disk” shock of an internal working surface. If we assume that the shock is strong (i. e., that it is highly supersonic and superalfvénic), from the Rankine-Hugoniot equations for MHD (e. g. Draine & McKee 1993) the post-shock radial cross section is given by :

$$\begin{aligned} P_w^{nr}(r) &= \frac{2}{\gamma + 1} \rho_0 v_0^2 \underline{\rho}(r) \underline{v}^2(r); \\ P_w^{rad}(r) &= \frac{(8\pi)^{1/2} \rho_0^{3/2} v_0 c_w^2 \underline{\rho}^{3/2}(r) \underline{v}(r)}{B_0 \underline{B}(r)}, \end{aligned} \quad (6)$$

$$\begin{aligned}\rho_w^{nr}(r) &= \frac{\gamma+1}{\gamma-1} \rho_0 \underline{\rho}(r); \\ \rho_w^{rad}(r) &= \frac{(8\pi)^{1/2} \rho_0^{3/2} v_0 \underline{\rho}^{3/2}(r) \underline{v}(r)}{B_0 \underline{B}(r)},\end{aligned}\tag{7}$$

$$\begin{aligned}B_w^{nr}(r) &= \frac{\gamma+1}{\gamma-1} B_0 \underline{B}(r); \\ B_w^{rad}(r) &= (8\pi)^{1/2} \rho_0^{1/2} v_0 \underline{\rho}^{1/2}(r) \underline{v}(r),\end{aligned}\tag{8}$$

where $P_w^{nr}(r)$, $\rho_w^{nr}(r)$ and $B_w^{nr}(r)$ are the post-shock gas pressure, density and magnetic field cross sections for the case of a non-radiative shock, and $P_w^{rad}(r)$, $\rho_w^{rad}(r)$ and $B_w^{rad}(r)$ are the cross sections for the case of a radiative shock in which the post-shock gas instantaneously cools to an isothermal sound speed c_w . As we have said above, equations (6-8) have been derived for the case of a strong shock. In order to obtain these relations it is also necessary to assume that the pre-shock Alfvénic Mach number has values smaller than $\sim M_w^2 = (v/c_w)^2$.

The factors including the specific heat ratio γ (see equations 6-8) take the numerical values $2/(\gamma+1) = 3/4$ and $(\gamma+1)/(\gamma-1) = 4$ for the case of a monoatomic, non-relativistic gas (i. e., for $\gamma = 5/3$). From now on, we will use these numerical values in order to simplify the equations.

Combining equations (6-8) with (1-2) we obtain the magnetic and gas pressure forces acting radially on the post-Mach disk material. The resulting magnetic force is

$$F_m^{nr} = \frac{4B_0^2}{\pi r_j} f_m^{nr}(r); \quad F_m^{rad} = \frac{2\rho_0 v_0^2}{r_j} f_m^{rad}(r),\tag{9}$$

where the dimensionless force $f_m(r)$ is given by

$$\begin{aligned}f_m^{nr}(r) &= -\underline{B}(r) \frac{r_j}{r} \frac{d}{dr} [r \underline{B}(r)]; \\ f_m^{rad}(r) &= -\underline{\rho}^{1/2}(r) \underline{v}(r) \frac{r_j}{r} \frac{d}{dr} [r \underline{\rho}^{1/2}(r) \underline{v}(r)].\end{aligned}\tag{10}$$

The resulting gas pressure force is

$$F_p^{nr} = \frac{3\rho_0 v_0^2}{4r_j} f_p^{nr}(r); \quad F_p^{rad} = \frac{(8\pi)^{1/2} \rho_0^{3/2} v_0 c_w^2}{r_j B_0} f_p^{rad}(r),\tag{11}$$

where the dimensionless force $f_p(r)$ is given by

$$f_p^{nr}(r) = -r_j \frac{d}{dr} [\underline{\rho}(r) \underline{v}^2(r)]; \quad f_p^{rad}(r) = -r_j \frac{d}{dr} \left[\frac{\underline{\rho}^{3/2}(r) \underline{v}(r)}{\underline{B}(r)} \right].\tag{12}$$

2.2. Scaling properties of the magnetic and gas pressure forces

Let us now consider the ratio M/P between the moduli of the magnetic and gas pressure forces. From equations (9) and (11) we obtain

$$(M/P)_{nr} = \frac{64}{3M_A^2} \left| \frac{f_m^{nr}(r)}{f_p^{nr}(r)} \right|; \quad (M/P)_{rad} = \frac{\sqrt{2}M_w^2}{M_A} \left| \frac{f_m^{rad}(r)}{f_p^{rad}(r)} \right|, \quad (13)$$

where $M_A \equiv v_0/v_A$ is the Alfvénic Mach number (obtained with the characteristic velocity v_0 and the Alfvén velocity $v_A = B_0/\sqrt{4\pi\rho_0}$), $M_w = v_0/c_w$ is the sonic Mach number (calculated with the characteristic velocity v_0 and the post-shock sound speed c_w of the radiative shock) and the $f_m(r)$ and $f_p(r)$ functions are given by equations (10) and (12), respectively.

One can argue that if the dimensionless cross section of the jet (described by equations 3-5) is smooth, then the $f_m^{nr}(r)$, $f_m^{rad}(r)$ and $f_p(r)$ functions (see equations 10 and 12) will have values of order 1.

In our derivation of the pressure force within the internal working surface, we have only considered the gradient of the post-shock gas pressure. Of course, the fact that the working surface material is free to leave through the sides of the jet beam will lead to an extra gas pressure gradient (directed outwards), particularly in the case of a non-radiative flow. The dimensionless pressure cross section due to this effect is still likely to lead to a dimensionless force $f_p(r) \sim 1$.

Setting $f_m^{nr}(r)$, $f_m^{rad}(r)$, $f_p^{nr}(r)$, $f_p^{rad}(r) \sim 1$, from equation (13) we then obtain

$$(M/P)_{nr} \sim \frac{64}{3M_A^2}; \quad (M/P)_{rad} \sim \frac{M_w^2}{M_A}. \quad (14)$$

From these two estimates of the ratio between the magnetic and gas pressure forces, we conclude that

- for the non-radiative case : if the Alfvénic Mach number of the flow entering the Mach disk is large (e. g., $M_A > 10$) we have $(M/P)_{nr} \ll 1$, and therefore the lateral expansion or contraction of the gas within the working surface will be governed by the gas pressure force,
- for the radiative case : if we consider jets with given values for v_A and c_w , it is clear that as the velocity v_0 increases, the $(M/P)_{rad}$ ratio increases (proportional to v_0). In particular, if we have flows with $v_A \sim c_w$, the magnetic to gas pressure force ratio has values $(M/P)_{rad} \sim M_w$. Thus, for a Mach disk in the strong shock regime, the post-shock magnetic pressure force will under most conditions dominate over the gas pressure force.

Therefore, for the non-radiative and the radiative cases, whether the jet material within the working surface expands or contracts in the radial direction will be determined by the signs of $f_p^{nr}(r)$ and $f_m^{rad}(r)$, respectively (see equations 10 and 12), provided that the Mach number of the jet has values $M_w \sim 10$ or larger.

3. Simulations of the internal working surface of an HH jet

Let us now consider the case of a jet model with a “top hat” density and velocity initial cross section, and an initial toroidal magnetic field cross section of the form

$$B(r) = B_0 \frac{r}{r_j}. \quad (15)$$

This kind of magnetic field cross section has been used in many of the previous simulations of radiative MHD jets (see, e. g., Gardiner & Frank 2000). With this cross section for the jet beam, we have

$$f_m^{nr} = -2r/r_j, \quad f_m^{rad} = -r_j/r, \quad (16)$$

and

$$f_p^{nr} = 0, \quad f_p^{rad} = \left(\frac{r_j}{r}\right)^2. \quad (17)$$

In other words, the magnetic pressure force is directed towards the axis, and the gas pressure force (acting in the radial direction on the working surface jet material) is zero for the non-radiative case, and points outwards for the radiative case.

We now compute models of a jet with this initial cross section, and an initial scale of the magnetic field $B_0 = 0$ (i. e., a purely hydrodynamic jet) and $B_0 = 5 \mu\text{G}$. The jet is injected with a constant density $n_j = 100 \text{ cm}^{-3}$, temperature $T_j = 900 \text{ K}$ and radius $r_j = 2 \times 10^{15} \text{ cm}$, and moves into a homogeneous, unmagnetized environment of density $n_{env} = 10 \text{ cm}^{-3}$ and temperature $T_{env} = 9000 \text{ K}$. The injection velocity varies sinusoidally with time, with a period $\tau = 20 \text{ yr}$, a half-amplitude of 150 km s^{-1} , and an average velocity of 300 km s^{-1} .

For the two chosen values of the magnetic field ($B_0 = 0$ and $5 \mu\text{G}$, see above and Equation 15), we run both non-radiative simulations and simulations in which we include the coronal ionization equilibrium cooling function of Dalgarno & McCray (1972). These simulations are run with the uniform grid, axisymmetric MHD code described in detail by De Colle & Raga (2006). The code uses a second order up-wind scheme, which integrates the MHD equations using a Godunov method with a Riemann solver. The Riemann problem is solved using primitive variables and the magnetic field divergence is maintained close to zero using the CT method (Tóth 2000). The computational domain of $(5, 1) \times 10^{16} \text{ cm}$ (axial, radial) extent is resolved with 2000×400 grid points. A reflection condition is applied on

the jet axis and on the $z = 0$ plane in the $r > r_j$ region. An outflow condition is applied in the remaining grid boundaries.

The time-dependent ejection velocity of the jet leads to the formation of successive internal working surfaces that travel down the jet flow. It is possible to estimate the ratio (M/P) between the magnetic and pressure forces within the internal working surfaces by noting that the shock velocity (associated with the two working surface shocks) has a value $v \approx 150 \text{ km s}^{-1}$. In other words, the value of the shock velocity is of the order of the half-amplitude of the ejection velocity variability (see, e. g., Raga et al. 1990).

With this value of v and the initial jet density and temperature, we can compute $M_A = v/v_A \approx 31$ (where $v_A = 4.8 \text{ km s}^{-1}$ for our $B_0 = 5 \mu\text{G}$ value and our initial jet density), $M_w = 150$ (for an assumed post-cooling sound speed of 10 km s^{-1}) and then we use equation (13) to obtain $(M/P)_{nr} \sim 0.02$ and $(M/P)_{rad} \sim 10^3$. Therefore, the magnetic force should have little effect in the non-radiative simulations, and result in similar structures for the internal working surfaces in the cases of magnetized and non-magnetized jets.

Figure 2 shows that our numerical simulations do show this effect. In this Figure, we show the density stratification obtained for non-radiative jets with $B_0 = 0$ (left) and $B_0 = 5 \mu\text{G}$ (right) after a $t = 90 \text{ yr}$ time-integration. It is clear that though the details of the flow are affected by the presence of a toroidal magnetic field, the general features of the two working surfaces produced within the computational domain are quite similar in the magnetized and non-magnetized cases.

The fact that $(M/P)_{rad} \sim 700$ (see above) implies that the magnetic pinch force should dominate the dynamics of the material within the internal working surfaces. Our two radiative numerical simulations (shown in Figure 3) do show this effect. In the magnetized simulation, the internal working surfaces become more strongly compressed towards the jet axis as they evolve (traveling away from the source), an effect not seen in the non-magnetized, radiative jet simulation (see Figure 3).

Figure 4 shows zooms of the knot situated at $z \approx 3.5 \times 10^{16} \text{ cm}$ (the knot on the top half of the $t = 90 \text{ yr}$ time frames shown in Figures 1 and 2) for our four computed models. This Figure shows that in the non-radiative case, the two working surface shocks have a separation which is similar to the diameter of the jet, and that the density structures are very similar for the $B_0 =$ and $5 \mu\text{G}$ models.

As expected, much higher densities are obtained in the radiative jet simulations. In the radiative case, the working surface obtained from the $B_0 = 5 \mu\text{G}$ model shows larger densities, a much higher concentration towards the jet axis and larger separations between the working surface shocks than the $B_0 = 0$ model.

More complex profiles for the magnetic field and the pressure were explored in the past by several authors (e.g. Gardiner & Frank 2000; Gardiner et al. 2000; Stone & Hardee 2000; O’Sullivan & Ray 2000; Frank et al. 2000; De Colle & Raga 2006), with results similar to the one obtained by the simple configurations of magnetic field and pressure presented here. As shown in Section 2.2, the expansion or contraction of the material in the working surface is nearly independent on the initial profile of the pressure. On the other side, the pre-shock magnetic field profile contributes to f_p^{rad} (but not to f_m^{rad}), and to the value of (M/P) . For small values of the magnetic field (e.g. close to the jet axis) $(M/P) \lesssim 1$, and the gas pressure force dominates.

Also, we note that Begelman (1998) has studied the development of pinch instabilities in non radiative jets, as due to the presence of a toroidal magnetic field. He found that a condition necessary for the development of the pinch instability is

$$\frac{d \ln B}{d \ln r} > \frac{\gamma\beta - 2}{\gamma\beta + 2}, \quad (18)$$

where $\beta = 8\pi P/B^2$. In the case of a radiative working surface with a post-shock region with $\beta \ll 1$ (corresponding to the condition $(M/P)_{rad} \gg 1$) this condition reduces to $F_m < 0$.

4. Conclusions

It is a known result that internal working surfaces in radiative, MHD jets with a toroidal magnetic field configuration form dense, axial structures, which do not appear in unmagnetized jets. We present a simple, analytic model with which we show that the strong jump conditions (applied to one of the working surface shocks) imply that the magnetic force dominates over the gas pressure force within a radiative working surface and that the gas pressure force is dominant for a non-radiative working surface (provided that one has a shock Mach number of at least $M_w \sim 10$ and an Alfvénic Mach number which does not exceed M_w^2).

Interestingly, the radial dependence of the toroidal magnetic field within a radiative working surface depends only on the cross section of the pre-shock ram pressure $p_{ram}(r) = \rho(r)v^2(r)$ impinging on the shocks. From equation (10), we can see that if we have a $p_{ram}(r)$ that decreases towards the edge of the jet faster than $1/r^2$, the magnetic force within the working surface will be directed outwards, and will tend to increase the width of the working surface.

We have run four simulations (with a top hat cross section for p_{ram} , that results in an axially directed magnetic pinch within the working surfaces), therefore in complete consistency with our analytic model. We find that in the non-radiative case the presence of a

toroidal magnetic field has very little effect on the structure of the internal working surfaces. We also find that for the radiative case, the presence of a toroidal magnetic field produces a strong axial compression of the material within the internal working surfaces (see Figure 4).

The analytic model presented in this paper can then be used to decide what ram pressure and toroidal magnetic field cross section to use in a magnetized, radiative, variable jet simulation in order to produce internal working surfaces that show narrower or broader structures than what is obtained in non-magnetized jet simulations. This might be a valuable tool when trying to model the knots in specific HH jets, and might provide a possible method for constraining the strength and the configuration of magnetic fields within such objects.

AR and AE acknowledge support from the DGAPA (UNAM) grant IN108207, from the CONACyT grants 46828-F and 61547, and from the “Macroproyecto de Tecnologías para la Universidad de la Información y la Computación (Secretaría de Desarrollo Institucional de la UNAM). This work is supported in part by the European Community’s Marie Curie Actions - Human Resource and Mobility within the JETSET (Jet Simulations, Experiments and Theory) network under contract MRTN-CT-2004 005592. We thank Enrique Palacios, Martín Cruz and Antonio Ramírez for supporting the servers in which the calculations of this paper were carried out.

REFERENCES

- Begelman, M. C. 1998, *ApJ*, 493, 291
- Cerqueira, A. H., de Gouveia Dal Pino, E. M., Herant, M. 1997, *ApJ*, 489, L185
- Cerqueira, A. H., de Gouveia Dal Pino, E. M. 1999, *ApJ*, 510, 828
- Cerqueira, A. H., de Gouveia Dal Pino, E. M. 2001a, *ApJ*, 550, L91
- Cerqueira, A. H., de Gouveia Dal Pino, E. M. 2001b, *ApJ*, 560, 779
- Dalgarno, A., McCray, R. A. 1972, *ARA&A*, 10, 375
- De Colle, F., Raga, A. C. 2006, *A&A*, 449, 1061
- Draine, B. T., McKee, C. F. 1993, *ARA&A*, 31, 373
- Frank, A., Ryu, D., Jones, T. W., Noriega-Crespo, A. 1998, *ApJ*, 494, L79
- Esquivel, A., Raga, A. C., De Colle, F. 2007, *A&A*, 468, 613

- Frank, A., Lery, T., Gardiner, T. A., Jones, T. W., Ryu, D. 2000, ApJ, 540, 342
- Gardiner, T. A., Frank, A. 2000, ApJ, 545, L153
- Gardiner, T. A., Frank, A., Jones, T. W., Ryu, D. 2000, ApJ, 530, 834
- Hartigan, P., Frank, A., Varnière, P., & Blackman, E. G. 2007, ApJ, 661, 910
- Masciadri, E., de Gouveia Dal Pino, E., Raga, A. C., Noriega-Crespo, A. 2002, ApJ, 580, 950
- O’Sullivan, S., & Ray, T. P. 2000, A&A, 363, 3550
- Raga, A. C., Binette, L., Cantó, J., Calvet, N. 1990, ApJ, 364, 601
- Raga, A. C., Velázquez, P. F., Cantó, J., Masciadri, E. 2002, A&A, 395, 647
- Stone, J. M., Hardee, P. E. 2000, ApJ, 540, 192
- Tóth, G. 2000, JCoPh, 161, 605

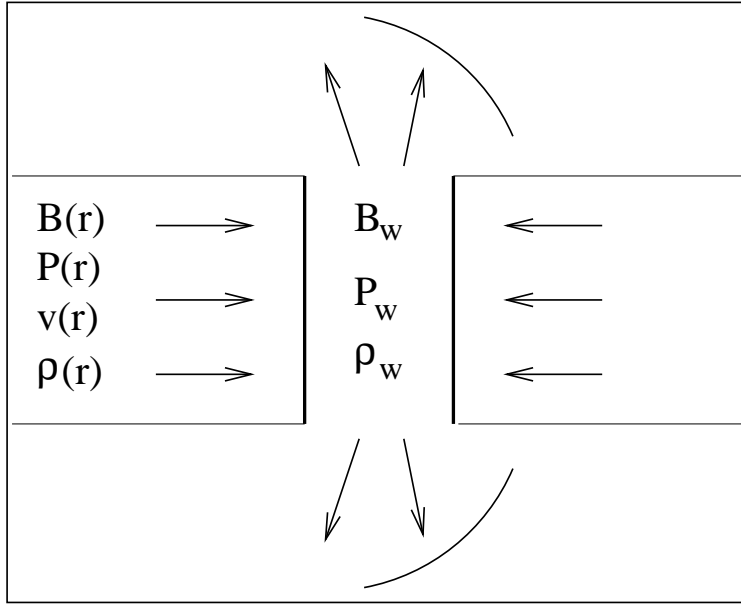


Fig. 1.— Schematic diagram showing an internal working surface produced by an ejection velocity variability (the source is to the left). In a frame of reference that moves with the velocity v_{ws} of the working surface, material from the continuous jet segments enters the shocked layer from both the upstream and downstream directions. The $B(r)$, $P(r)$, $v(r)$, $\rho(r)$ radial cross section of the pre-shock region produces a $B_w(r)$, $P_w(r)$, $\rho_w(r)$ cross section within the shocked layer (in this shocked layer, the velocity along the jet axis is ~ 0 in the reference frame moving with the working surface). The material in the working surface exits laterally, shocking against the jet cocoon.

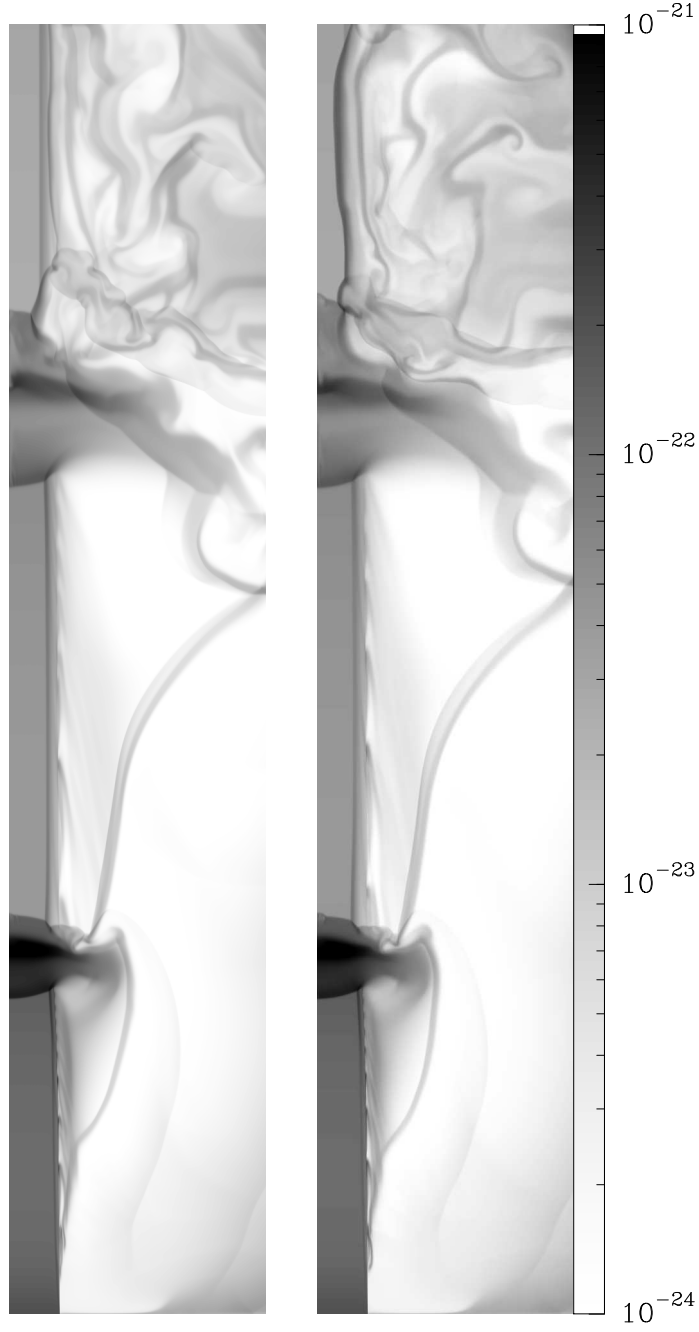


Fig. 2.— Density structures resulting from $t = 90$ yr time integrations of the non-magnetized (left) and magnetized (right) non-radiative jet models. The flow is injected from the bottom of the grid, and travels upwards, producing internal working surfaces (two of these are seen in the displayed time frames). The frames cover the full, $(5, 1) \times 10^{16}$ cm (axial, radial) computational domain. The densities are shown with the logarithmic gray scale given (in g cm^{-3}) by the bar on the right.

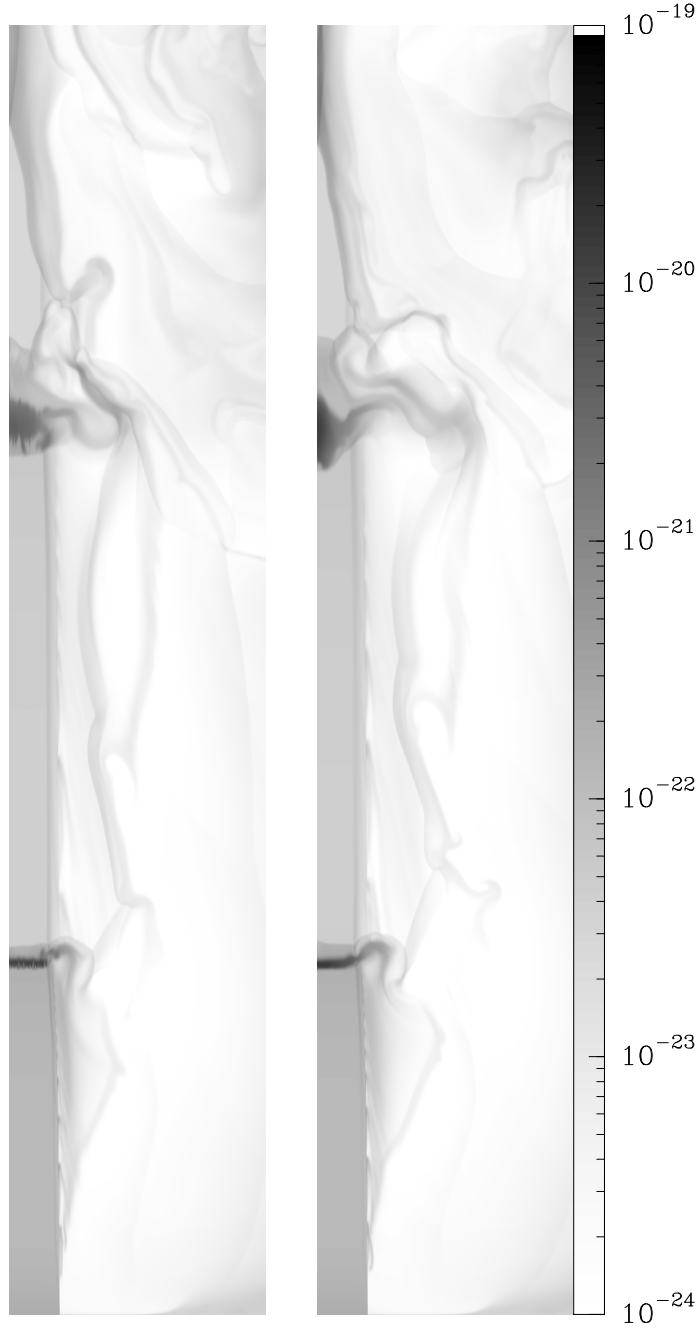


Fig. 3.— Density structures resulting from $t = 90$ yr time integrations of the non-magnetized (left) and magnetized (right) radiative jet models. The frames cover the full, $(5, 1) \times 10^{16}$ cm (axial, radial) computational domain. The densities are shown with the logarithmic gray scale given (in g cm^{-3}) by the bar on the right.

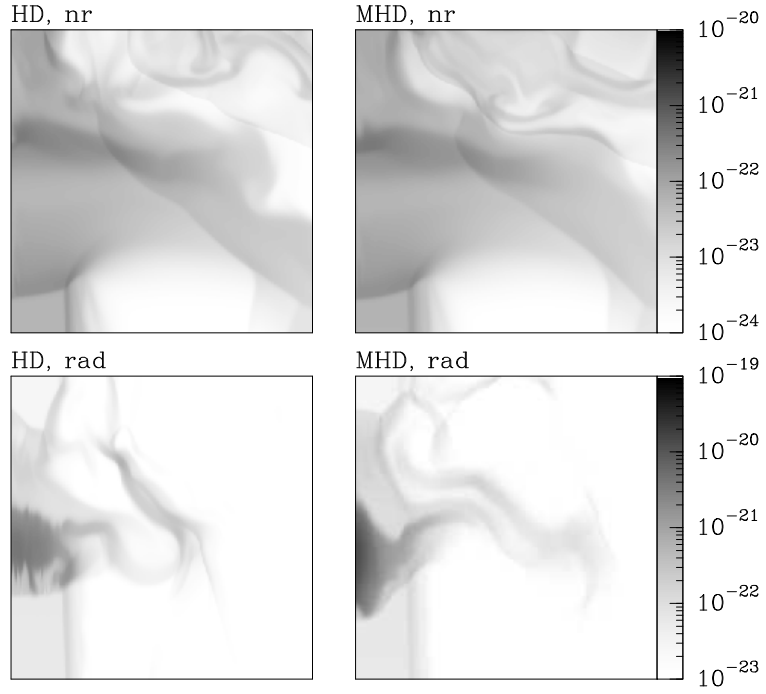


Fig. 4.— Density stratifications of the knot seen in the upper half of the $t = 90$ yr time frames shown in Figures 2 and 3. The non-radiative models are shown on the top, and the radiative models on the bottom. The non-magnetized models are on the left, and the magnetized ones on the right. The displayed domain has an axial and radial size of 7.5×10^{15} cm. The density of the non-radiative models is given (in g cm^{-3}) by the bar on the top right, and the density of the radiative models by the bar on the bottom right.